Spray drying of colloidal suspensions: Coupling of particle drying and transport models with experimental validations

Jean-Marc Schweitzer, Marion Servel, Fabien Salvatori, Aurélie Dandeu, Marine Minière, Jean-François Joly, Quentin Gaubert, Séverine Barbosa, F. R.A. Onofri

PRE-PRINT
Jean-Marc Schweitzer, Marion Servel, Fabien Salvatori, Aurélie Dandeu, Marine Minière, Jean-François Joly, Quentin Gaubert, Séverine Barbosa, Fabrice R.A. Onofri,
Spray drying of colloidal suspensions: Coupling of particle drying and transport models with experimental validations,
Chemical Engineering Research and Design, Volume 170, 2021, Pages 224-238, ISSN 0263-8762, https://doi.org/10.1016/j.cherd.2021.04.004.

Spray drying of colloidal suspensions: coupling of particle drying and transport models with experimental validations

Jean-Marc Schweitzer[1,*], Marion Servel[1], Fabien Salvatori[1], Aurélie Dandeu[1], Marine Minière[1], Jean-François Joly[1], Quentin Gaubert[1,2], Séverine, Barbosa[2], Fabrice R.A. Onofri[2]

[1] IFP Energies nouvelles, 69360 Solaize, France

[2] Aix-Marseille Université, CNRS, IUSTI, UMR 7343, 13453 Marseille, France

* *Corresponding authors: jean-marc.schweitzer@ifpen.fr, fabrice.onofri@univ-amu.fr*

Abstract

A numerically effective approach was developed for the modeling of spray-drying of colloidal suspensions. This approach was based on the integration of two models. The first is a phenomenological and radially symmetric model accounting for the drying of single-droplets, while the second employs computational fluid dynamics (CFD) simulations to account for the gas flows conditions and atomization in a spray dryer. Experiments were also conducted on single suspension droplets trapped in an acoustic field as well as on droplets in a mini-spray dryer. The predictions of the models were found to be in reasonable agreement with the experimental data, in terms of droplet shrinking and buckling, particle yield, and spatial distribution in the spray dryer mockup.

Keywords:

Spray drying, drying kinetics, colloidal suspensions, crust formation, particle yield, computational fluid dynamics, acoustic levitation.

1 Introduction

Spray drying technology is commonly used in numerous process industries. It is extensively used for food processing, as well as in polymer, pharmaceutical, and porous material engineering, to obtain powders composed of solid particles with well-defined characteristics, such as particle morphology, size distribution, porosity, and density (Bonazzi and Dumoulin, 2014; Cheow et al., 2010; Cotabarren et al., 2018; Fu et al., 2013; Langrish, 2007; Langrish and Fletcher, 2003; Lintingre et al., 2016; Sen et al., 2010; Singh and Van den Mooter, 2016; Sosnik and Seremeta, 2015; Sperling and Gradzielski, 2017; Walton and Mumford, 1999). Among the many droplet-to-particle drying patterns, three typical behaviours can be distinguished (Lefebvre and McDonell, 2017; Walton and Mumford, 1999). In the first one, the sprayed droplets tend to form a "skin" at their surface (which is generally the case with polymers); in the second, the droplets are susceptible to crystallization (if there are dissolved components); and in the third, the droplets show an agglomerative tendency (which is the case with colloidal suspensions). This study was focused on the third behaviour.

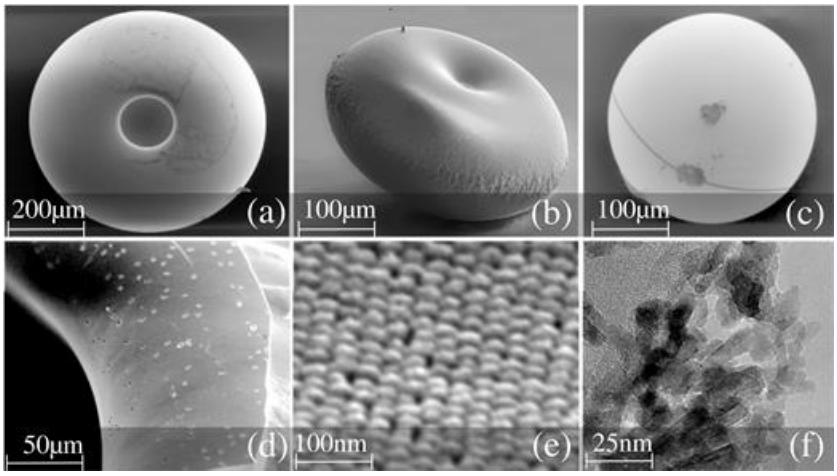

Figure 1 (a-d): Scanning electron and (f) transmission electron images of particles formed by: the drying of (a, b, d) suspension droplets of quasi-monodisperse silica nanoparticles (zoomed in (e)), (c) a suspension droplet of boehmite nanoparticles (zoomed in (f)).

In the spray drying process of colloidal suspensions, the solid nanoparticles, suspended in an aqueous solvent, are sprayed with an assisted nozzle into a chamber, which is supplied with an additional hot gas flow. The droplets are transported by the gas, while getting dried. The nanoparticle agglomerates (henceforth referred to as just "particles") and are essentially collected at the bottom of the spray chamber when the solvent within the droplets is fully vaporized (see Figure 1). The control of both unit operability and outlet particle properties requires a thorough understanding (possibly through modeling) of various complex phenomena, which include: (i) interaction of the gas and solid flows in the chamber; (ii) drying mechanism at the particle scale; (iii) particle–particle collisions; and (iv) particle adhesion on the walls. In the next paragraphs, we briefly review and understand how these phenomena are fundamental.

The interaction of gas and solid flows in a spray chamber (i) is intrinsically linked to the spray chamber geometry, gas injection, and the suspension injection nozzles. All these parameters have significant effects on the particle residence time. The modeling of particle transport in a gas flow requires extensive computational fluid dynamics (CFD) calculations, based either on the Euler–Euler or Euler–Lagrangian methods, e.g., (Poozesh et al., 2018).

Mezhericher et al (2010) overviewed the various approaches for modeling of droplet drying kinetics. The identified models were suitable for droplets with insoluble solids, dissolved solids or both types of solid content. They classified these approaches into four different categories: semi-empirical models, utilizing the concept of characteristic drying curve; deterministic drying models describing the processes within the droplet with momentum, energy, and specie conservation; deterministic models coupling distribution of solid component described by population balance; and, finally, reaction engineering methods. During the first stage, the nanoparticles in the suspension agglomerate as the droplets shrink, until they form a crust on the droplet surface, e.g.,

(Cheow et al., 2010; Fu et al., 2013; Lauga and Brenner, 2004; Onofri et al., 2013; Style and Peppin, 2010; Yarin et al., 2002). In the second stage, depending on the rigidity of the crust, the particles (i.e., solid shells with a liquid core) remain spherical, but continue to dry at a constant volume. Alternatively, their shape can start to deviate from being spherical owing to the deformation (buckling) of their crust (Lintingre et al., 2015; Lintingre et al., 2016; Pauchard and Couder, 2004; Sen et al., 2012; Tirumkudulu, 2018); see Figure 2. Walker et al. (1999) discuss the effect of inter-particle forces on the buckling phenomenon. According to their model, strong repulsive forces between colloids will tend to a bifurcation between droplet shrinking and buckling phenomena. Conversely, attractive inter-particle forces will help to conserve the droplet spherical shape along the complete drying process. The shrinking and buckling processes have a significant influence on the gas–solid friction forces, flow conditions, and particle yield of the spray drying unit (Jubaer et al., 2018). The particle–particle collision effects are usually considered minimal, compared to the particle–wall bouncing (iii), and specifically, the particle sticking and droplet wetting effects (iv), e.g., (Ali et al., 2015). In fact, the droplet–droplet and particle–particle collisions have a lower probability for the divergent sprays used in spray dryers. However, the quality of the spray created by the nozzle(s) and the fouling of the walls are considered as key parameters, governing the yield of industrial spray dryers, e.g., (Sirignano and Edwards, 2000).

A literature review of spray dryer models for practical relevance to operating problems reveals a great variability of complexity. Full spray dryer models were classified according to their complexity by Oakley (Oakley, 2004) and ranked models into four levels ranging from simple heat and mass balances (level 0), Heat and Mass Balances with solid-vapor equilibrium (level 1), Rate-based with simplifying assumptions about particle motion Level 2A and Rate-based with simulation of gas flow and particle motion obtained from CFD (Level 2B). Despite the recent developments in the CFD modeling of spray dryers, e.g.,

(Cotabarren et al., 2018; Pinto et al., 2014; Poozesh et al., 2018), the operating conditions required to obtain powders with well specified properties, such as morphology and specific area, e.g. (Walton, 2000) are still essentially established through an empirical approach (i.e., trial and error). Such an approach is not only time consuming, but also often inadequate for scaling up the process systems and pilot plants, and for extensive parametric studies. Thus, any affordable and efficient modelling approach that takes into account the basic particle drying mechanisms and the hydrodynamics in the spray chamber is highly desirable.

With this perspective, the present work proposes an efficient numerical model that accounts for the drying process at the droplet scale, and the interactions and transport phenomena at the scale of the spray dryer unit. The numerical results and discussions were supported by experiments carried out on boehmite and silica colloidal suspensions using a mini spray dryer (B-290, BÜCHI) and an evaporating chamber equipped with an integrated acoustic trap. Both the experimental systems allow controlling the experimental operating conditions required for spray drying studies in different ways. The remainder of this paper is organized as follows. After this introduction section, Section 2 describes the key features and operating modes of the two experimental setups, i.e., the acoustic trapping experiment and the mini spray dryer. Section 3 presents the coupled models referred to as the droplet drying and spray drying models. The former accounts for the drying of a single droplet in five steps (droplet shrinking, crust formation, buckling and drying, core reduction, and thickening), while the latter accounts for the spray dryer geometry, atomization and gas flow conditions. Section 4 discusses and compares the experimental and numerical results, while Section 5 provides the concluding remarks with perspectives.

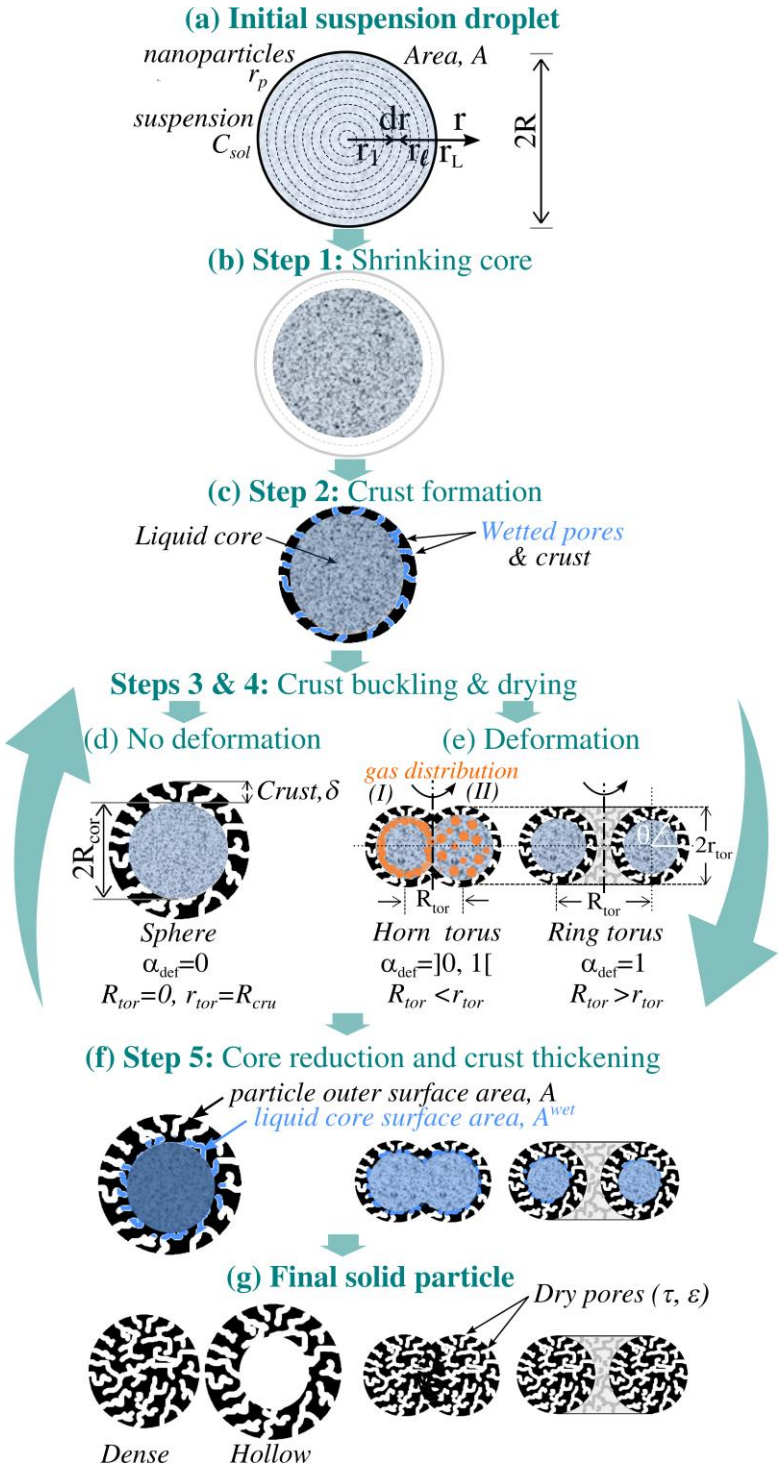

Figure 2: Schematic diagram of the droplet drying model in five steps: (1) shrinking droplet; (2) crust formation and (3) crust buckling; (4) drying of the particle and (5) particle core reduction and crust thickening.(a,b) Initial conditions are supposed to be uniform (no continuous gradients) and the particle spherical with radius R. (c) Spherical particle with a liquid core and a crust with wetted pores. Depending on the drying conditions, the particle remains (d) spherical

or it adopts a (e) horn or ring torus shape. These three shapes are distinguished with the morphological parameter α and two characteristics radiuses, r_{tor} and R_{tor}. The gas within the liquid core can be distributed either (I) peripherally or (II) homogenously. The final particle can be spherical, horn or ring torus shaped, as well as (f) dense or hollow.

2 Experimental setups and procedures

2.1 Single droplet in an acoustic trap

To study the drying of a single droplet, a droplet levitation method was chosen over the other methods, e.g., (Daubersies, 2012; Hu and Larson, 2002; Lauga and Brenner, 2004), to limit the effects (e.g., surface contamination and triple line) that are not relevant for spray drying studies. Among the different methods for levitating a single particle (acoustic, hydrodynamic, electrostatic, magnetic, and optical) (Brenn et al., 2007; Jakubczyk et al., 2013; Maconi et al., 2018; Onofri et al., 1995; Onofri et al., 2015; Saha et al., 2010; Sperling and Gradzielski, 2017; Yarin et al., 1998; Yu et al., 2013), the acoustic levitation was found to be the most flexible to trap and characterize both spherical and non-spherical particles in a gaseous flow, whose sizes typically range from one mm, down to a few tens of micrometers.

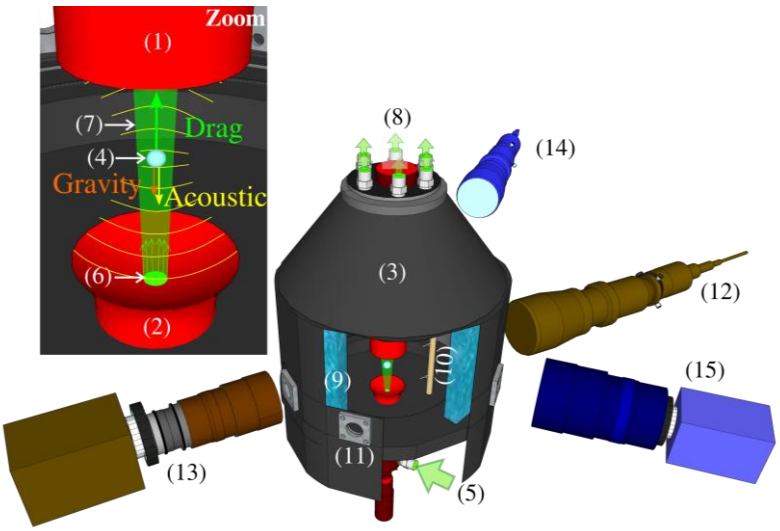

Figure 3: Experimental setup (not to scale) of drying of a suspension droplet in acoustic levitation: (1) acoustic transducer; (2) acoustic reflector; (3) evaporation chamber; (4) droplet; (5) gas inlet; (6) millimeter-sized circular orifice; (7) laminar gas-jet with a nearly flat profile at the droplet location and scale; (8) gas outlet; (9) double-walled water heating path; (10) thermocouples; (11) optical windows; (12) emission of the shadowgraph; (13) detection of the shadowgraph; (14) emission of the PIV system; (15) detection of the PIV system.

However, this method also suffers from some drawbacks, such as acoustic streaming effects(i.e induced recirculations, Gaubert, 2017; Yarin et al., 1999), which need to be corrected or minimized. The experimental facility, specially developed for this study, is shown in Figure 3. It was built around an ultrasonic levitator (1–2), operating at 100 kHz (i.e., a wavelength of 3.2 mm). The levitator is enclosed in an evaporation chamber (3). A suspension droplet (4) is trapped slightly below a pressure node of the acoustic field. In fact, this standing acoustic field is the superimposition of a travelling wave produced by the acoustic transducer (1) and a counter travelling wave reflected by the parabolic reflector (2). This reflector (with a convergent internal profile) was designed with a metal 3D printer (Gaubert, 2017).

Prior to starting the experiments, the temperature (T) and relative humidity (RH) within the chamber are set with a controlled evaporation and mixing (CEM) system (not shown in the Figure) (Gaubert, 2017). This CEM allows, via the inlet (5) and a circular hole in the reflector (6), the generation of a vertical laminar jet of dry steam (7), which is blown on the droplet. This jet subsequently exits at the top of the chamber (8). It is worth noting that this acoustic trap is operated upside down, compared to the usual acoustic levitators. This configuration helps stabilize the droplet position by a distance of a few hundred micrometers, when the drag force induced by the jet increases. Thus, the droplet can stay in equilibrium under the action of three major external forces, namely gravity, drag, and acoustics (from the incident and reflected acoustic waves). The evaporation chamber, with a double wall

water heating system (9) and thermocouples (10) distributed vertically, is also equipped with eight optical windows (11). The latter allows the introduction of a relative humidity sensor (not shown) into the chamber, as well as the introduction of the droplet in the trap. It also facilitates the optical diagnostics. For the present study, two optical diagnostic systems are setup, a particle image velocimetry (PIV, 12–13) system to characterize the gas velocity field around the droplet, and a shadowgraph (13–14) for imaging the backlighted droplet. The shadowgraph measures the size of the droplet or the particle with a subpixel resolution (Fdida and Blaisot, 2010; Onofri and Barbosa, 2012), provided it is a spherical or spheroidal object (Onofri et al., 2015). The PIV results (Gaubert, 2017), obtained by seeding the gas jet by smoke from incense (Melling, 1997), have shown that the jet is laminar, in a first approximation, with a nearly flat velocity profile at the position and scale of the droplet. The initial droplet Reynolds number (Re) investigated was in the range of 106 – 230, corresponding to a local gas velocity of 1.66 – 3.6 m/s. Note that for a droplet Re greater than 106, the jet would cause the advection of the eddies generated by the acoustic streaming, e.g., (Ali Al Zaitone and Tropea, 2011; Yarin et al., 1999). Owing to the limitations of the transducer electronics, the temperature range within the chamber is limited to 20 – 65 °C. Depending on the temperature, its relative humidity can be adjusted between 2.5% and 95%. In this study (Gaubert, 2017), experiments were conducted with two types of aqueous suspensions — one containing colloidal silica beads (Klebosol™, from AZ Electronic Materials), and the second, irregularly shaped boehmite particle (Pural SB3, an aluminum oxide hydroxide prepared in-house) in different concentrations. These colloids differed especially, in their nanoparticle shapes and particle size distribution (PSD), see Figure 1 (e–f). The silica beads were almost perfectly spherical and quasi-monodisperse with a radius $r_{sol}(\pm\sigma) = 25 \pm 3\,nm$ (Onofri et al., 2013), while the boehmite nanoparticles were mostly irregularly shaped and elongated with $r_{sol}(\pm\sigma) = 9 \pm 6\,nm$ (Gaubert, 2017).

2.2 Spray in a mini spray dryer

The mini spray drying experiment was built around a mini spray dryer B-290, commercialized by BÜCHI Labortechnik AG. Figure 4 shows the key components of this laboratory mock-up, extensively studied and documented in the literature, e.g., (Cheow et al., 2010; Cotabarren et al., 2018; Pinto et al., 2014). It allows producing droplets, of a few tens of micrometers in diameter, which are composed of aqueous or non-aqueous suspensions. This system was operated in an open mode, i.e., the atmospheric air was heated up and transported to the drying chamber and then vented back into the atmosphere. This device allows adjusting the gas temperature up to 220 °C for a maximum air flow of 35 m^3/h. The nozzle was assisted with nitrogen up to 0.4 m^3/h at 5.5 bar. As the residence is very limited in this device (close to 1 s), we will assume constant temperature and humidity based on logarithmic average between the inlet and the outlet.

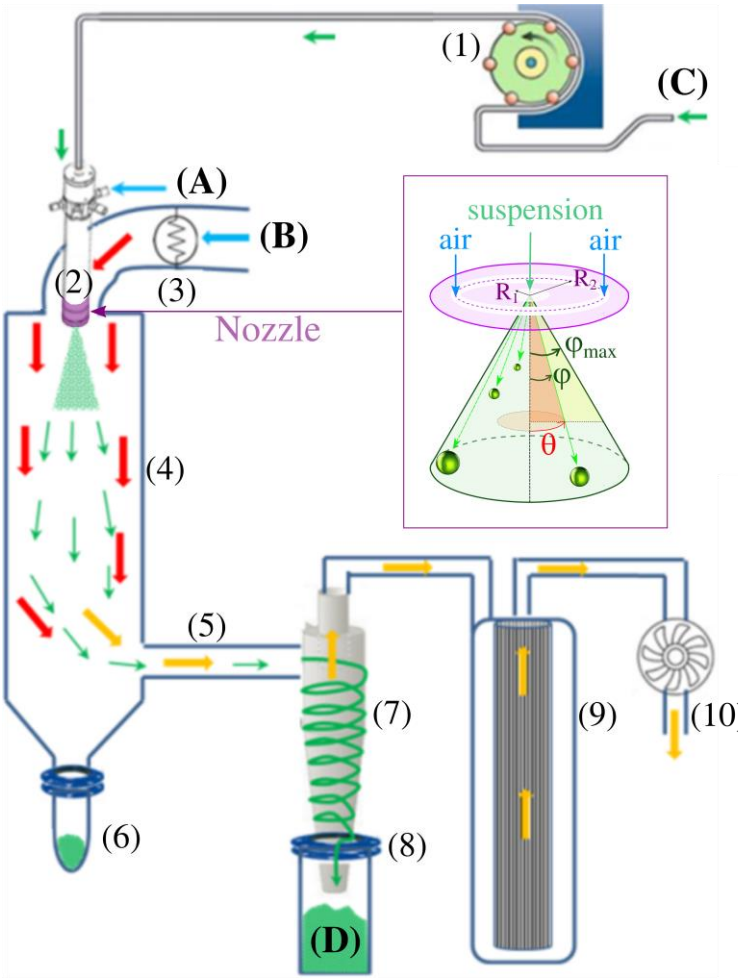

Figure 4: Experimental setup: schematic of the mini spray dryer B-290. Materials: (A) additional gas injection; (B) nozzle gas supply; (C) suspension supply; and (D) collected powder. Technical parts include (1) peristaltic pump; (2) assisted nozzle; (3) gas heater; (4) drying chamber; (5) outlet; (6) collection pot of the drying chamber; (7) cyclone separator; (8) powder main collection pot; (9) gas filter; (10) extraction fan. The zoomed inset is of the spray cone geometry.

3 Modeling

Different types of particles drying models are described by Poozesh et al. (2018) according to their complexity. Simplest models describe an homogeneous droplet where only average properties are calculated like overall water content. Due to their low computing time, coupling with complex hydrodynamics is facilitated. Those models cannot predict

crust formation due to solid concentration radial profile nor particle buckling. On the other hand, more complex particle drying models ware developed taking into account the droplet shrinking, the crust formation and the prediction of buckling phenomena. In the case of crystallization phenomena, several authors have coupled those complex models with a population balance in order to predict the nucleation and the growth of solid particles (Handscomb et al., 2009a; Handscomb et al., 2009b). The model developed in this work is close to Handscomb's approach without taking into account the population balance (no crystallization phenomena).

3.1 Drying droplet model

3.1.1 Droplet shrinking and formation of the first crust (Steps 1 and 2)

We consider a single droplet, initially spherical and homogeneous. The experimental conditions are uniform (i.e no gradients in temperature and species concentrations). In the drying process of this droplet, the first observation is a shrinking, characterized by an isotropic reduction of its radius (see Figure 2). In most practical situations of interest, the hypothesis of homogeneity of the properties of the droplet is not valid. In fact, the evaporation of the water at the droplet surface induces a solid concentration profile within the droplet. This is particularly the case when the Peclet number (Pe) of the droplet exceeds unity,

$$Pe = \frac{1}{D_{sol}} \frac{R\partial R}{\partial t} > 1, \quad (1)$$

where R is the radius of the droplet and D_{sol} is the diffusion coefficient of the solids (i.e., nanoparticles), within the suspension forming the droplet, calculated using a modified Stokes–Einstein equation in order to account for the solid concentration effect (Sobac et al.,2020). To calculate the solid concentration profile within the droplet, we discretize

the droplet along the droplet radius in concentric layers of equal thickness. The radial transport of solids into the droplet is expressed through Fick's diffusion law, which reduces, for a spherically symmetric object (Crank, 1975), to:

$$\frac{dn_{sol}}{dt} = 4\pi D_{sol} \frac{\partial}{\partial r}\left(r^2 \frac{\partial C_{sol}}{\partial r}\right) \tag{2}$$

where n_{sol} is the local number of moles of solid in a layer of thickness dr at a radial coordinate r; C_{sol} is the local molar concentration of solid;. Eq. (2) is accompanied by two boundary conditions for the solids, namely no diffusion at the center ($r = 0$) and outside ($r = R$) of the droplet; that is,

$$D_{sol} \cdot \left.\frac{\partial C_{sol}}{\partial r}\right|_{r=0} = 0$$

$$D_{sol} \cdot \left.\frac{\partial C_{sol}}{\partial r}\right|_{r=R} = 0 \tag{3}$$

This equation is numerically solved using a finite difference approach. The effect of internal circulation on evaporation of fluid droplets containing nano-sized particles caused by viscous effects at the liquid–gas interface in the convective environment is not investigated in this work. The internal circulation is expected to increase the effective particle diffusion and leads to the concept of effective Peclet number (Wei et al, 2016). In this work, the contribution of internal circulation will be encompassed in the maximum solid concentration determining the crust formation, especially since we are working at high Peclet values.

At a constant volume, the diffusion of solids induces a counter-diffusion of the liquid water. A volume flow balance must be valid for each layer of volume V_{lay}:

$$\frac{dV_{lay}}{dt} = 0 = \frac{d(V_{wat} + V_{sol})}{dt} = \frac{d\left(\frac{n_{wat} M_{wat}}{\rho_{wat}} + n_{sol} M_{sol}/\rho_{sol}\right)}{dt}$$

(4)

where V_{wat} and V_{sol} are the volumes of liquid water (subscript wat) and solids (subscript sol) in a given layer, respectively; n_{wat} and n_{sol} are the corresponding number of moles; M_{wat} and M_{sol} are the molecular weight of the liquid water and solid, respectively; and ρ_{wat}, ρ_{sol} are the corresponding densities. From Eq. (4), the variation in the number of moles of water in the liquid state within a layer is

$$\frac{dn_{wat}}{dt} = -\frac{\rho_{wat}}{\rho_{sol}}\frac{M_{sol}}{M_{wat}}\frac{dn_{sol}}{dt} \quad (5)$$

Water emerges as vapor from the droplet outer layer. At this interface, the water vapor in the external gas mixture is assumed to be in thermodynamic equilibrium with its condensed state. The water vapor pressure is deduced from the vapor pressure of free water $P_{wat}^{vap,free}$, and the activity coefficient of water a_w: $P_{wat}^{vap,sat} = \frac{P_{wat}^{vap,free}}{a_w}$ (Fu et al., 2011). with subscript sat for saturation. The dependency of vapor pressure of free water on temperature can be modeled with the Antoine's equation, $P_{wat}^{vap,free} = A - B/T$ where, for instance, $A \approx 13.7 mmHg$, and $B \approx 5120\ mmHg.°C$ for T=[20,70]°C. The activity coefficient of water depends moderately on the nature of the solids and their concentration; however it depends exponentially on the temperature through the relation $a_w = a_0 \exp[-E_b/(R_{gas}T)]$ (Blandamer et al., 2005). As an example, for the boehmite suspension used later, the constants $a_0 \approx 1850$ and $E_b \approx 20\ kJ.mol^{-1}$ were estimated experimentally.

During drying, the droplet rapidly heats to the wet-bulb temperature (T_d), and its temperature remains constant whilst the surface remains saturated with moisture (Handscomb et al. 2009). A second drying period begins when moisture can no longer be supplied to the surface at a rate sufficient to maintain saturated conditions. The transition between these two regimes occurs at the critical moisture content and may also coincide with the beginning of crust formation (Cheong et al., 1986). In

this work, we will not account for that change of temperature after the crust formation phase.

The molar water balance in the outer layer is :

$$\left.\frac{dn_{wat}}{dt}\right|_{r=R} = -k_{gs} 4\pi R^2 \left(C_{wat}^{vap,sat} - C_{wat}^{gas}\right) \quad (6)$$

where k_{gs} is a gas–liquid mass transfer coefficient (Walzel and Furuta, 2011) and C_{wat}^{gas} is the concentration of water-vapor in the atmosphere surrounding the droplet. Using the gas constant R_{gas}, the molar water balance at the droplet surface can be written as

$$\left.\frac{dn_{wat}}{dt}\right|_{r=R} = -k_{gs} 4\pi R^2 \left(\frac{P_{wat}^{vap,sat}}{R_{gas} T_d} - C_{wat}^{gas}\right) \quad (7)$$

To estimate k_{gs}, a correlation deduced for a particle in a fluid flow is used (Couderc, 2017). This correlation, valid for droplet with Reynolds numbers in the range [10-10^3] , is expressed in terms of the Sherwood (Sh), Schmidt (Sc) and Reynolds (Re) numbers of the droplet. With $Sh = (2 + 0.6Re^{1/2}Sc^{1/3})$ (Pinto et al., 2014; Ranz and Marshall, 1952), this correlation can be written as

$$k_{gs} = \alpha_{gs} \frac{D_{wat}^{vap}}{d_p} \left(2 + 0.6Re^{1/2}Sc^{1/3}\right) \quad (8)$$

where D_{wat}^{vap} is the diffusion coefficient of water vapor in the surrounding atmosphere and α_{gs} is an additional correcting factor that is adjusted experimentally in the acoustic trap experiment (Gaubert, 2017).

In this work, a numerical discretization was used considering that all layers are of equal and constant thickness, except the outer one. The thickness of this layer must vary with the evaporation of water. This

implicit time dependency of the outer layer thickness is written as follows:

$$dr|_{r=R} = \frac{V_{wat} + V_{sol}}{4\pi R^2} \quad (9)$$

where V_{wat} and V_{sol} are the volumes of the liquid water and solids contained in this layer. The new radius of the droplet (at time t) is obtained by summing up all thicknesses as $R = \int_0^R dr$. At this stage, there is only solids and liquid water in the droplet; therefore, the volumes of water and solid in each layer are recalculated from the corresponding number of moles as $V_{wat} = (n_{wat}M_{wat})/\rho_{wat}^{liq}$ and $V_{sol} = (n_{sol}M_{sol})/\rho_{sol}$. For the solid and liquid water concentrations in a layer, we use the relations $C_{sol} = n_{sol}/V_{lay}$ and $C_{wat} = n_{wat}/V_{lay}$.

The condition of formation of the first crust is defined by a limit solid concentration within the suspension, which is $C_{sol} \geq C_{sol}^{lim}$. This condition can also be expressed in terms of a limit suspension density, $\rho_{sus} \geq \rho_{sus}^{lim}$, where $\rho_{sus}^{lim} = \rho_{wat} + M_{sol}C_{sol}^{lim}(1 - \rho_{wat}/\rho_{sol})$. When the crust is not yet formed, it is necessary to control the water quantity contained in the outer layer at each calculation step. In practice, when $n_{wat}^R \approx 0$ the total number of layers is decreased by one, to account for the droplet shrinking. On the other hand, when the crust formation limit conditions are reached in the outer layer, the droplet size reduction is to be blocked (i.e. rigid crust and evaporation at constant volumes). To do so, the number of layers is then simply fixed when the conditions $C_{sol} \geq C_{sol}^{lim}$ or $\rho_{sus} \geq \rho_{sus}^{lim}$ are first fulfilled. At the end of Step 2, the particle is composed of a liquid core (remaining suspension) surrounded by a hardening mantle (growing crust).

3.1.2 Crust drying (Step 3)

During this step, the water remaining in the crust is progressively evaporated. As in Steps 1 and 2, the external transfer can be characterized by an external transfer coefficient k_{gs}. In fact, the

evaporation of water is now a combination of the internal diffusional transport through the pores of the crust, visible in the Figure 5, and the external mass transfer towards the surrounding atmosphere. The diffusion of water vapor through the dry pores is modeled with an apparent transfer coefficient k_{gs}^{app}, defined as the ratio of the molecular diffusion of water vapor in free space to the product of thickness δ and mean tortuosity τ of the dry zone of the crust, $k_{gs}^{app} = D_{wat}^{vap}/(\tau\delta)$ (Reuge and Caussat, 2007). Finally, a global transfer coefficient k_{gs}^{glo} that accounts for the decrease of the wetted area A^{wet} of the crust, in contact with the dry zone of the crust, can also be introduced (Figure 5).

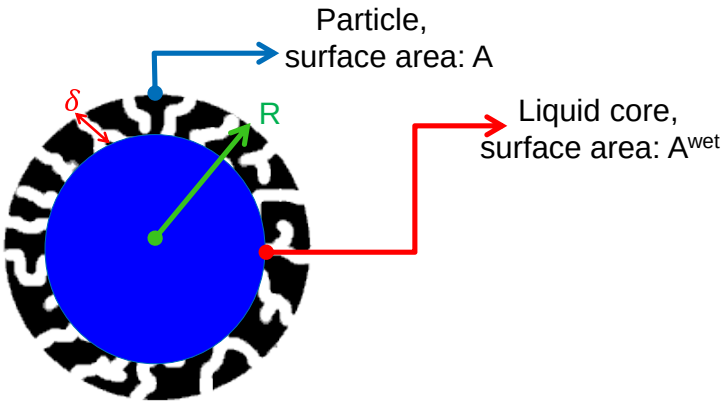

Figure 5: Liquid core shrinking after crust formation

Assuming that the quantity of water vapor accumulated in the pores and in the outer film is negligible (with respect to total mass balance), the molar water flowrate exiting out of the particle surface (subscript $_{surf}$) reads as,

$$k_{gs}A^{wet}\left(C_{wat}^{surf} - C_{wat}^{gas}\right) = k_{gs}^{app}A^{wet}\left(\frac{P_{wat}^{vap,surf}}{R_{gas}T_d} - C_{wat}^{gas}\right)$$
$$\approx k_{gs}^{glo}A\left(\frac{P_{wat}^{vap,sat}}{R_{gas}T_d} - C_{wat}^{gas}\right) \quad (10)$$

with $A^{wet} = 4\pi(R-\delta)^2\varepsilon = A(1-\delta/R)^2\varepsilon$; δ being the thickness of the dry zone; ε being the crust average porosity; and A being the total surface area of the particle. The global transfer coefficient is derived from Eq. (10) as

$$\frac{1}{k_{gs}^{glo}} = \frac{\delta}{\varepsilon(D_{wat}^{vap}/\tau)(1-\delta/R)^2} + \frac{1}{k_{gs}} \quad (11)$$

In the previous equation, the term $\varepsilon(D_{wat}^{vap}/\tau)$ is the water vapor diffusivity in the dry zone of the crust (Reuge and Caussat, 2007). Finally, the molar flow rates equations (2) and (5) remain valid for the core with the following boundary condition for the global transfer of water at the core surface:

$$\left.\frac{dn_{wat}}{dt}\right|_{r=R_{core}} = -k_{gs}^{glo} 4\pi R^2 \left(\frac{P_{wat}^{vap,sat}}{R_{gas} T_d} - C_{wat}^{gas}\right) \quad (12)$$

Step 4 ends when the crust is completely dry and the menisci in the pores reach the liquid core of the particle.

3.1.3 Core reduction and crust thickening (Step 5 and iterations with Steps 3 and 4)

Once the crust is dried, the water remaining in the core continues to evaporate. If there is a deformation of the crust, it does not necessarily result in a gas inlet (Step 3). However, if the droplet shape evolution is mechanically blocked by the rigidity of the crust, the water released by the liquid core must be compensated for by some gas inlet from the surrounding atmosphere. In the latter case, three phases (water, solid, and gas) are present at the same time in the core, and an iteration between Steps 3 and 5 needs to be performed. To account for this effect on the core (i.e. all layers of index l such that $L_l \leq R_{cor}$), Eq. (2) must be corrected by a gas holdup ε_{gas} for the gas in the core:

$$\frac{dn_{sol}}{dt} = 4\pi D_{sol} \frac{\partial}{\partial r}\left((1-\varepsilon_{gas}) r^2 \frac{\partial C_{sol}}{\partial r}\right) \quad (13)$$

with the following boundary conditions:

$$D_{sol}\left.\frac{\partial C_{sol}}{\partial r}\right|_{r=0} = 0$$

$$D_{sol}\left.\frac{\partial C_{sol}}{\partial r}\right|_{r=R_{cor}} = 0 \quad (14)$$

The gas flowrate that enters within the core (dV_{gas}/dt) is expressed as a function of the volumetric flowrate of liquid water leaving the core:

$$\frac{dV_{gas}}{dt} = (1-\alpha_{def})\ k_{gs}^{glo}\ 4\pi R^2\left(\frac{P_{wat}^{vap,sat}}{R_{gas}T_d} - C_{wat}^{gas}\right)\frac{M_{wat}}{\rho_{wat}} \quad (15)$$

At this stage, two scenarios (a and b, see Figure 2) are envisaged for the distribution of the gas into the core In scenario (a), the gas is distributed peripherally and the core receives the gas flow, as given by $d\varepsilon_{gas}/dt = (dV_{gas}/dt)/(4\pi R_{core}^2 dr)$, when $r = R_{core}$; and $d\varepsilon_{gas}/dt = 0$ when $r < R_{core}$. In scenario (b), the gas is homogenously dispersed within the core, and the temporal variation of the gas retention is constant along the core radius, as dictated by

$$d\varepsilon_{gas}/dt = (dV_{gas}/dt)/\left(\int_0^{R_{core}} 4\pi R_{core}^2 dr\right)$$

for $r = [0, R_{core}]$. Note that the gas retention rate $\varepsilon_{gas} = V_{gas}/V_{tor}$ is directly related to the porosity (Johnson et al., 2019).

Writing the liquid water balance in the core requires accounting for the counter-diffusion of solids and gas for the two scenarios; for scenario (a):

$$\left.\frac{dn_{wat}}{dt}\right|_{r=R_{core}} = -\frac{\rho_{wat}}{\rho_{sol}}\frac{M_{sol}}{M_{wat}}\frac{dn_{sol}}{dt} - \frac{V_{lay}\rho_{wat}}{M_{wat}}\frac{d\varepsilon_{gas}}{dt}$$

$$\left.\frac{dn_{wat}}{dt}\right|_{r<R_{core}} = -\frac{\rho_{wat}}{\rho_{sol}}\frac{M_{sol}}{M_{wat}}\frac{dn_{sol}}{dt} \quad (16)$$

and for scenario (b):

$$\left.\frac{dn_{wat}}{dt}\right|_{r\leq R_{core}} = -\frac{\rho_{wat}}{\rho_{sol}}\frac{M_{sol}}{M_{wat}}\frac{dn_{sol}}{dt} - \frac{V_{lay}\rho_{wat}}{M_{wat}}\frac{d\varepsilon_{gas}}{dt} \quad (17)$$

When the concentration of the solids in the outer layer reaches the limit C_{sol}^{lim}, in Step 5, the crust thickens again and the number of layers discretizing the core is reduced by one. This process is repeated until the core completely dries up.

3.1.4 Case of particle shape deformation during crust drying

In this section, the particular case of particle shape deformation from a sphere to a torus is modeled from a geometrical point of view. In other words, the buckling phenomenon is not predicted but the deformation is simulated depending on a deformation coefficient determined experimentally (Gaubert, 2017). In a further work, this parameter can be correlated to a buckling criterion as proposed in the work of Timoshenko (1936).

After Steps 1 and 2, when the crust is still thin, the outlet flow of the liquid water can induce the buckling (Step 3) of the particle and the entry of gas within the liquid core (Step 4). The modeling of the crust deformation is a complex problem (Miglani and Basu, 2015) that is tackled in a simple way in this present work. With our radial model, we can evaluate its influence on the kinetics of the drying by introducing some a priori information from the experiments. The ring-torus-shaped particles (see Figure 1 and Figure 2) are commonly reported in the literature, and were essentially observed in our experiments with silica suspensions. For boehmite suspensions, most of the particles observed were spherical to spindle-torus shaped (Gaubert, 2017). When the crust is formed, the flowrate of liquid water leaving the particle (due to evaporation) can be compensated by gas entering into the particle and / or by a change in particle volume due to its deformation from a spherical to a toric shape. The balance between both phenomena is obtained by introducing a weighted deformation coefficient (α_{def}) =

[0,1]. Therefore, the variation of particle volume (V_{tor}) in time and the gas flowrate entering into the particle can be determined as follow:

$$dV_{tor}/dt = -\alpha_{def} Q_{wat}^{vap}$$

$$dV_{gas}/dt = (1 - \alpha_{def}) Q_{wat}^{vap} \quad (18)$$

Where Q_{wat}^{vap} is the volumetric flowrate of liquid water vaporized (in m^3/s) determined as follow:

$$Q_{wat}^{vap} = k_{gs} A_p \left(\frac{P_{wat}^{vap,sat}}{R_{gas} T_d} - C_{wat}^{gas} \right) \frac{M_{wat}}{\rho_{wat}} \quad (19)$$

In geometry, a torus is a surface of revolution generated by revolving a circle in three-dimensional space about an axis that is coplanar with the circle (see Figure 6).

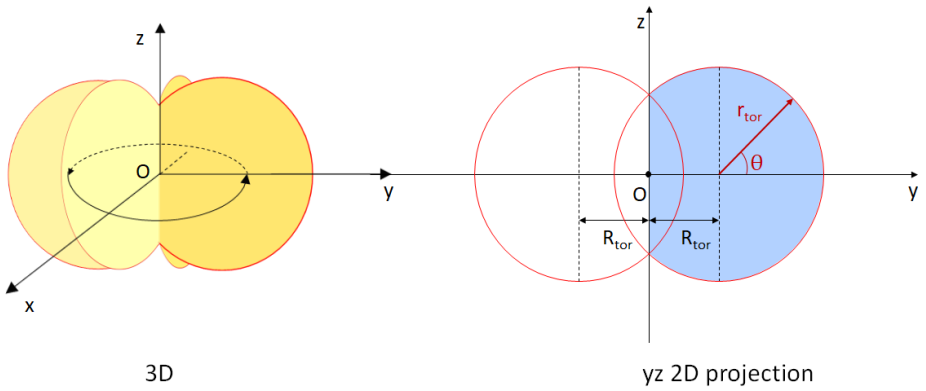

Figure 6: Torus geometry

According to the values of R_{tor} and r_{tor}, it is possible to describe all the intermediates shapes between a sphere and a ring torus (see Figure 7).

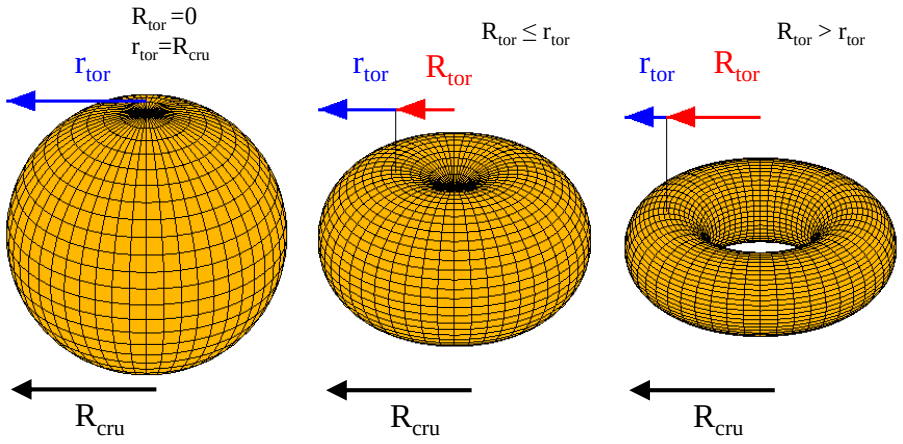

Figure 7: Intermediate shapes between a sphere and a torus as a function of R_{tor} and r_{tor}

The volume of all intermediate particle shapes between a sphere and a torus can be calculated as follow:

$$\begin{cases} & R_{tor} + r_{tor} = R_{cru} \\ \text{if } R_{tor} \le r_{tor}, & V_{tor} = 2\pi\left[R_{tor} r_{tor}^2\left[\theta_l - \frac{\sin(2\theta_l)}{2}\right] + \frac{2}{3} r_t^3 \sin^3(\theta_l)\right] \\ \text{if } R_{tor} > r_{tor}, & V_{tor} = 2\pi^2 r_{tor}^2 R_{tor} \end{cases} \quad (20)$$

with $\theta_l = \pi - \text{Acos}\left(\frac{R_{tor}}{r_{tor}}\right)$

Given that the system of equations Eq (18) allows to calculate at each time the particle volume V_{tor} after the first crust formation, one can deduce the temporal evolution of R_{tor} and r_{tor} solving the system of equations Eq (20).

3.1.5 Isothermal hypothesis testing

Our model assumes the isothermal of the droplets and the particles during the drying process. To evaluate the validity of this hypothesis, let us consider a particle in a surrounding drying gas at atmospheric pressure, saturated in water vapor. The maximum heat flux for water

evaporation is $k_{gs}P_{sat,T}^{free}L_{wat}/(R_{gas}T)$, where L_{wat} is the (latent) heat of vaporization of water. The maximum conductive flux inside the particle can be estimated by a linear approximation of the Fourier's law, $\emptyset_{con} = \lambda(\Delta T/R)$. If all the evaporative heat flux is driven by the droplet, then $\Delta T/T = k_{gs}P_{sat,T}^{free}L_{wat}/(R_{gas}T)$. For example, when T=353.15K and R = 500 μm, we find that with $\Delta T/T = 0.002$ (i.e., approximately 0.1K over 353.15K). Thus, the temperature gradient within the particles and droplets is effectively negligible.

3.2 Spray dryer model

As a first step, this model uses an Eulerian approach to determine the gas flow properties within the spray drying chamber. Then, these calculations are combined with the droplet drying model using a Lagrangian approach, which injects and tracks the suspension droplets, individually and sequentially.

We will consider only the gas flow without any disturbance due to particle motion. This assumption seems acceptable for this lab tool because of the low liquid volume fraction, and a small droplet size distribution. For bigger dryer, it will not the case anymore and it will be necessary to take into account a better coupling for mass and energy.

3.2.1 Gas flow

The general gas flow field in the chamber is calculated by solving the Navier–Stokes equations with the finite element method (using COMSOL Multiphysics® 5.3a). For the turbulence, the V2-f model is used (Laurence et al., 2005). Briefly, the latter contains two more equations in addition to the classical κ–ε model (Launder, 1972). The first equation describes the transport of the turbulent velocity fluctuations normal to streamlines and the second equation accounts for the non-local effects, such as the wall-induced damping of the turbulent kinetic energy (Jubaer et al., 2018). Owing to the symmetry of the dryer geometry only half of its geometry is simulated. The global flow

behaviour is conserved by imposing symmetrical boundary conditions. The spray dryer geometry is also decomposed in three parts, the gas flow inlet system (an assister coaxial nozzle) (Cotabarren et al., 2018); the spray dryer chamber itself; and the gas outlet (only partly visible in the bottom right corner of Figure 12). All the dimensions are those of the BÜCHI B-290 mini spray dryer (e.g., spray chamber with a cylindrical (cyl) body with a height H_{cyl} = 0.42 m and diameter D_{cyl} = 0.14 m; bottom cone (con) with a height h_{con} = 0.05 m; and a gas outlet with a cylindrical T-junction located 0.04 m above the conical part). In the same way, the gas inlet has a classical coaxial and annular shape with inner and outer radiuses R_1 = 0.015 mm and R_2 = 0.035 mm, respectively (see Figure 4).

3.2.2 Spray simulation

Atomization is a complex process (Lebas et al., 2009) and is not modeled in the present work. Instead, the droplets are injected at the top of the chamber, with a stochastic procedure, in a cone, with a size distribution, whose parameters were estimated from experiments carried on the mini-spray dryer B-290. Numerically, this is realized with four random numbers. The first one determines the diameter of each suspension droplet injected. This diameter follows a Rosin-Rammler PSD (RR-PSD), i.e., a classical two parameter distribution with a probability density function $\mathrm{PSD(D)} = \mathrm{n(D^{n-1}/D_c^n)exp[-(D/D_c)^n]}$, where D_c and n stand for the particle characteristic size and the PSD uniformity constant, respectively. In the remainder of this paper, these size distributions shall be referred to as RR-PSD(D_c, n). The injection velocity of the droplets is considered to be uniform, with V = 100 m/s, based on the mini-spray dryer specifications. The second and third random numbers are used in selecting the droplet trajectory azimuthal θ=[0, 2π] and polar $\varphi = [0, \varphi_{max}]$ angles; see Figure 4(a); $\varphi_{max} = 30°$ is the half-cone angle of the full cone spray.

3.2.3 Droplet trajectories and collisions

The droplet momentum equation account for the evolution of the mass and dynamics of a single droplet along its trajectory, and their form is as follows:

$$m(t)\frac{d\vec{v}}{dt} = \overrightarrow{F_f} + m(t)\,\vec{g} \tag{21}$$

with

$$\left\|\overrightarrow{F_f}\right\| = \frac{1}{2}\rho_g\, C_D\, \frac{\pi\, d_p^2}{4}\, \left\|\overrightarrow{\vartheta_{slip}}\right\|^2$$

and

$$\overrightarrow{\vartheta_{slip}} = \overrightarrow{\vartheta_g} - \overrightarrow{\vartheta_s}$$

$$C_D = \frac{24}{Re_P} \text{ for } Re_p<1 \text{ and } C_D = \frac{18.5}{Re_p^{0.6}} \text{ for } 1< Re_p <1000$$

$$Re_p = \frac{\rho_g \left\|\overrightarrow{\vartheta_{slip}}\right\| d_p}{\mu_g}$$

where ϑ_{slip}stands for the particle slip velocity with respect to the surrounding gas and C_D is the drag force coefficient.

Droplet–droplet collisions and spray-induced turbulence are neglected; however, collisions with the cylindrical and conical walls of the dryer are modeled. An elastic rebound (total reflection) is assumed for particles with a crust. A sticking (or more precisely wetting) process is assumed for the liquid droplets. The coupling of the resulting gas flow field with the droplet injection, transport, interaction with the walls, and their drying kinetics, is implemented in Fortran 90 computer language.

4 Results and discussions

4.1 Single droplet and droplet drying model

Experiments on the drying of a single droplet in levitation were conducted on droplets of silica and boehmite suspensions (Gaubert, 2017), for a relative humidity of 2.5% (to limit the harmful streaming

effects), a temperature of 29 to 51 °C (see Figure 10), and gas-jet velocities (V_{jet}) ranging from 1.66 to 3.60 m/s. This range of parameters is well below the drying conditions encountered in the industry, but it is the price to pay for obtaining detailed experimental data.

For these conditions, Pe of the initial droplets was approximately 10, while the Re was within the range 106 – 230. However, it should be noted that Re increased during the course of the experiment (with a reduction in the droplet size). For the numerical simulations, the initial number of layers was set to 50, as a good trade-off among the computational efforts, resolution, and numerical dispersion. The later comes from the finite difference method and notably the second-order central difference in the diffusion term, with error magnitude $O(d_r^3)$. The other fixed (known a priori) parameters of the simulations were $\alpha_{def} = 1$, estimated from the particle image analysis; and $\tau \approx 2.75 \pm 0.25$, estimated with a classical mercury porosimetry analysis of the collected powder. The diffusivity of the nanoparticles was estimated using the Stokes–Einstein equation.

Figure 8 illustrates a typical evolution, in three parts, for the normalized particle surface area $A(t)/A(t=0)$ versus time. The 4π coefficient in front of time t is a normalization term used in the well-known $D^2 - law$ evaporation models, e.g., (Ranz and Marshall, 1952). As noted, we first observed a linear decay (with slope β) of the particle area. It was followed by a transition zone, the start of which indicated crust formation, and the end of which corresponded generally to particle buckling (if present). The third part is similar to a plateau, slightly decreasing in buckling, and corresponding to the particle drying.

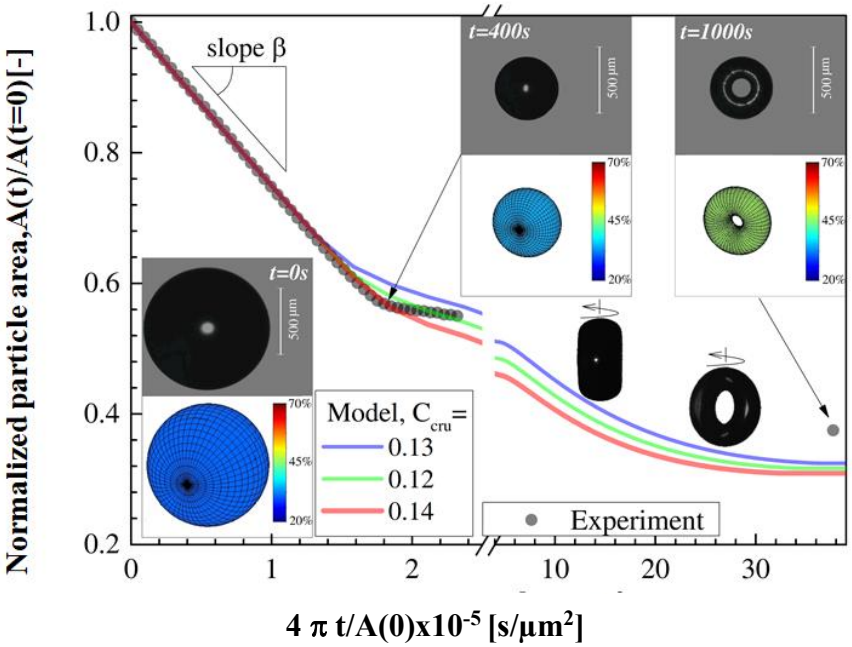

Figure 8: Comparison of the temporal evolution of the particle total area: results from experiments under acoustic levitation versus predictions of the droplet drying model (for three values of the concentration limit C_{sol}^{lim} for the crust formation). The shadowgraph images are compared with the predictions of the model (color coding: mass concentration in solids, in %). Conditions: silica suspension, $\boldsymbol{R(0) = 481\mu m}$, T=42°C, RH=2.5%, ***and*** $\boldsymbol{V_{jet} = 1.96\ m.s^{-1}}$.

These behaviours, including the transition from spherical to ring-torus shape ($\alpha_{def} = 1$), were systematically observed for all silica suspensions (i.e., all investigated temperatures, gas-jet velocities, and initial volume fraction in silica beads, $C_{sol}^{vol} = 0.0032$ to 0.16). For boehmite suspensions and the same conditions (except that $C_{sol}^{vol} = 0.0082$ to 0.04), the evaporation curves were found to be similar; however, the final particle remained almost spherical ($\alpha_{def} \approx 1$) when Re < 106, and they adopted a horn torus shape (with $\alpha_{def} \approx 0.8$) when Re > 106 (Gaubert, 2017). Note that, in the acoustic trap, non-spherical particles tended to rotate on their own vertical axis (as depicted in Figure 8). We believe that this slow rotation (approximately 1 – 2 Hz) had a negligible influence of the evaporation process. However, this rotation was a concern for optical diagnoses. In fact, with the shadowgraph system, the

parameters of the torus-shaped particle could not be measured, when the particle were not exactly facing the camera, which explains the large blank space in part 3 of Figures 8.

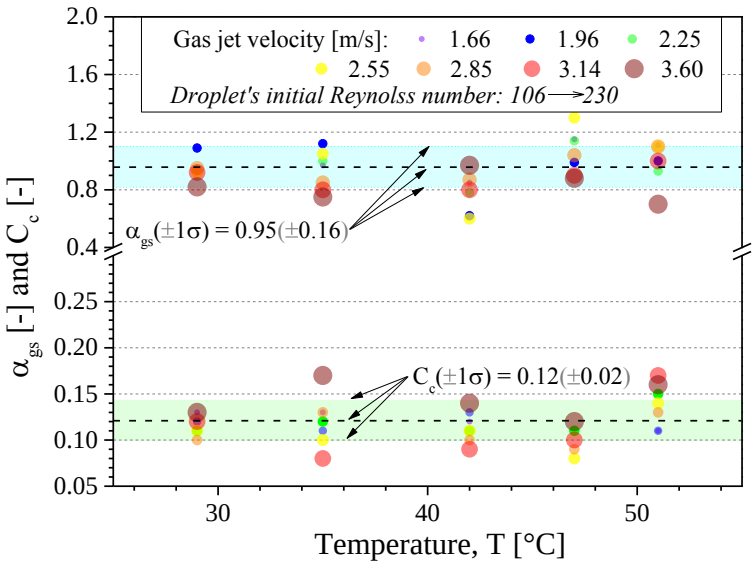

Figure 9: Experimental estimation of the gas–liquid mass transfer correction factor α_{gs} ***and*** C_{sol}^{lim} ***for the formation of the first crust. Fixed parameters: silica suspension,*** $\boldsymbol{R(0) = 464\mu m}$, T=29°C, RH=2.5%, ***and*** V_{jet}=1.66 m.s^{-1}.

Figure 9 presents the experimental estimation of α_{gs} and C_{sol}^{lim} in the case of silica suspensions with various concentrations. Both coefficients were obtained by comparing, with a classical iterating and minimizing method, the experimental data for different temperatures and gas-jet velocities, and the predictions of the droplet drying model. In the present case, i.e., for silica suspensions, the optimal values were found to be $\alpha_{gs}(\pm1\sigma) = 0.95(\pm0.16)$ and $C_{sol}^{lim}(\pm1\sigma) = 0.12(\pm0.02)$. Revisiting Figure 9, it is clear that the value $C_{sol}^{lim} = 0.12$ allowed retrieving the basic features of the experimental curve, even though the description of the drying zone (slow decaying plateau) was not completely satisfactory with regard to the experimental values. For boehmite suspensions, we found that $C_{sol}^{lim}(\pm1\sigma) = 0.12(\pm0.04)$. Both values differed significantly from the values obtained on samples in a tray dryer, $C_{sol}^{lim}(\pm1\sigma) = 0.25(\pm0.01)$ for silica and $C_{sol}^{lim}(\pm1\sigma) = 0.30(\pm0.01)$ for boehmite

suspensions. A plausible explanation for this apparent discrepancy is that both methods do not detect the formation of the crust at the same stage, a point that should be clarified in a future work.

Figure 10 compares the slopes of the linear part of the evaporation curves obtained experimentally (β_{exp}), with those from the simulations (β_{mod}), obtained using the droplet drying model. A comparable agreement, while slightly worse, was found for boehmite suspensions (Gaubert, 2017). β is the slope of the simplified D^2 model, currently used to represent step 1 (shrinking core), because it has a linear evolution. We can observe a perfectible accuracy (Figure 10) between β_{exp} et β_{mod} that justifies the interest to use the model developed in paragraph 3. Overall, the predictions of the droplet drying model were found to be reasonably satisfactory over the entire range of parameters studied. This was particularly true for the first part of the drying process.

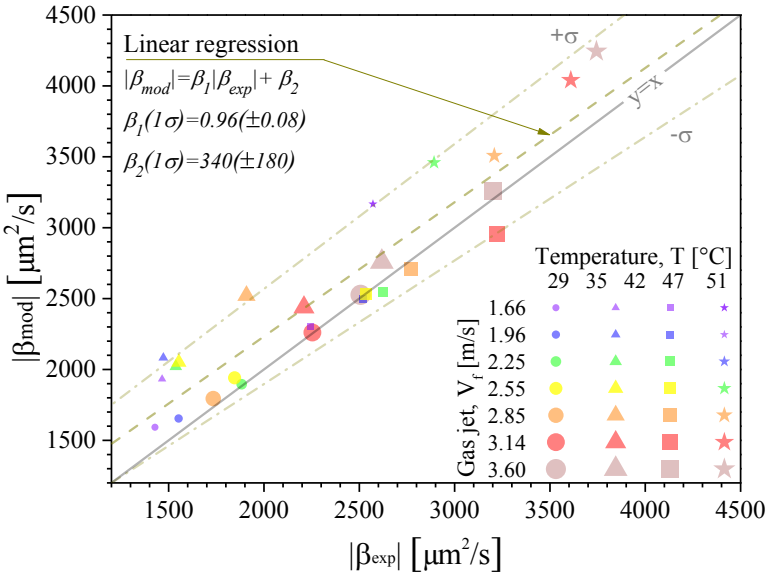

Figure 10: Comparison of the slope β of the linear part of the evaporation curves obtained experimentally with those simulated with the droplet drying model. Parameters are same as those mentioned in Figure 9.

4.2 Mini spray and spray drying model

All experiments with the mini spray dryer B-290 were carried-out for a maximum gas flow temperature of 200 °C, a relative humidity of 2.5%, and a gas flowrate (fixed by the manufacturer) of 30 $m^3.h^{-1}$. The gas flow injected simultaneously with the suspension through the nozzle is not considered in the simulations as it is only representing one percent of the total inlet gas flow. Two boehmite suspensions were sprayed with a fixed flowrate of 0.44 $L.h^{-1}$. The PSDs of the droplets sprayed were estimated to be of RR-type, with parameters (30, 1.5) and (40, 1.5), from the spray dryer data sheet and correlations from the literature (Lefebvre and McDonell, 2017); see Figure 11. Their initial velocity was also estimated to be of 100 $m.s^{-1}$. For the calculations and the present operating conditions, α_{def} was set to 0.8 after analyzing different experimental samples.

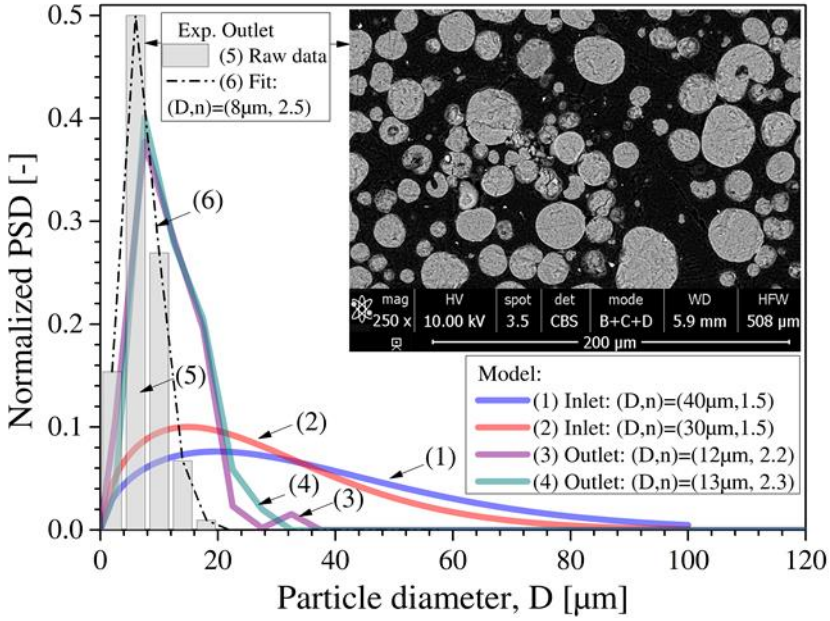

Figure 11: Spray drying of boehmite suspension: comparison of the PSDs for a gas flowrate of 30 $m^3.h^{-1}$. (1–2) Initial RR-PSDs of sprayed droplets: (D, n) = (40, 1.5) and (30, 1.5), respectively. (3–4) corresponding PSDs that were numerically predicted for the particles exiting the dryer (the fitting parameters were provided for comparison purpose). Inset: typical SEM image; and (5–6) corresponding particle size histogram and fit for the particle sample collected in case (4).

For the simulations, a constant temperature across the spray dryer chamber was assumed, even though a decrease of approximately 30 °C from the atomizer to outlet regions was observed experimentally. In these conditions, the Peclet number of the droplets was approximately 10, which corresponded to a diffusion regime. The droplet temperature was almost constant and remained below the ebullition temperature. Figure 12 shows some cross-sectional views illustrating the gas flow structure and particle trajectories within the spray chamber, for three values of the gas flow rate, 2, 10, and 30 $m.s^{-1}$ (experimental conditions). The asymmetry induced by the outlet was clear. The increase in the gas recirculation and droplet path lengths (and thus, the resident time) with the gas flow rate was also evident.

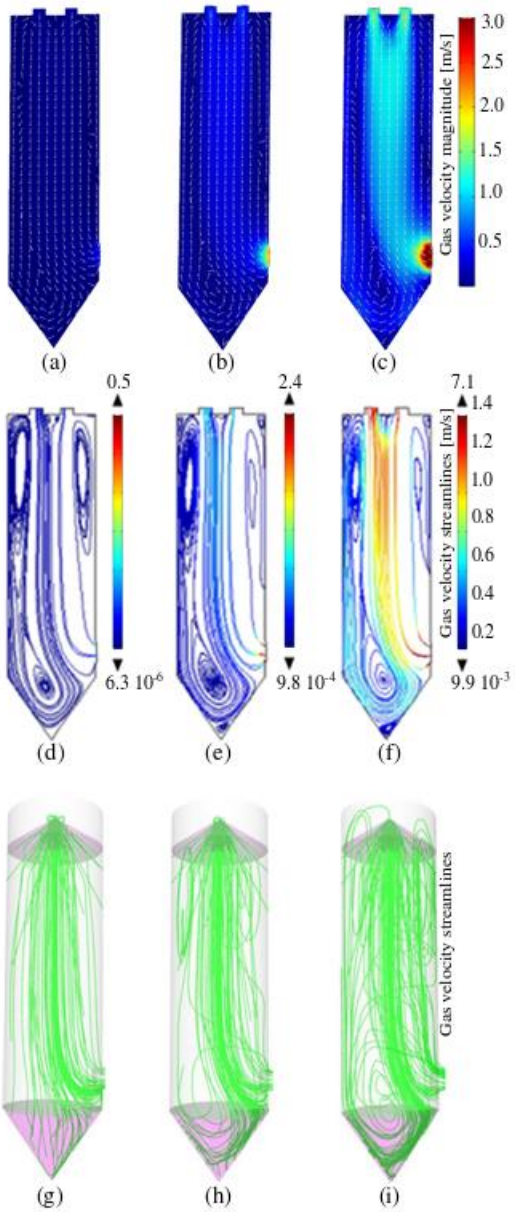

794 ***Figure 12: Complete simulations for three gas flow rates: (a, d, g) 2 $m^3.h^{-1}$; (b, e, h) 10 $m^3.h^{-1}$; and (c, f, i) 30 $m^3.h^{-1}$ for RR-PSD = (30,***
796 ***1.5). (a–c) gas velocity field and (d–f) corresponding streamlines. Color coding was based on the velocity magnitude. The values were***
798 ***constrained into rigid limits for better visualization of the velocity variations (real limits are indicated at the top and bottom of each bar).***
800 ***(g–i) Examples of a few droplet trajectories.***

802 Regarding the complexity of the flow structure and the polydispersity of the droplets generated by the atomizer, it is necessary

to evaluate the number of droplets that need to be tracked numerically to obtain reliable statistics. To this end, Figure 13 shows the numerical estimation of the particle mass fractions (yields), in the atomizer region, spray dryer outlet, and on the walls of the spray dryer chamber, versus the number of droplets sprayed, for a gas flowrate of 30 m^3/h (corresponding to a mean velocity of nearly 3 m/s) and RR-PSD of (30, 1.5).

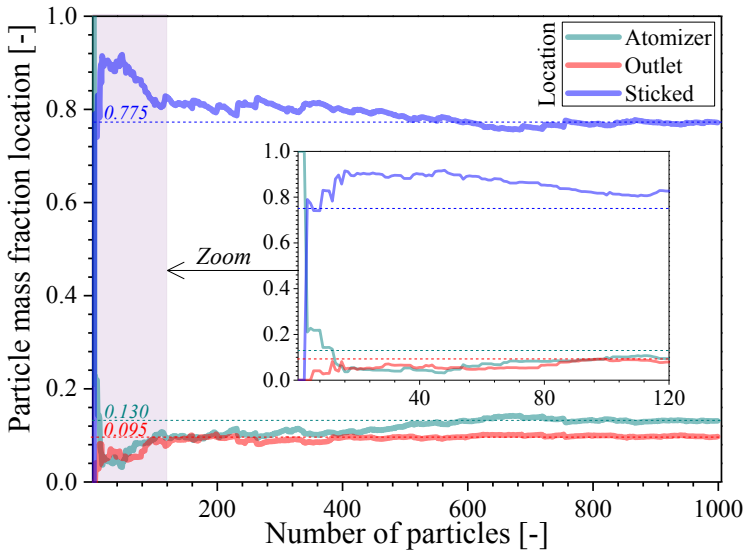

Figure 13: Convergence plots of the calculations versus the number of droplet trajectories (Lagrangian particle tracking) simulated. Distribution of the particle mass fraction (yield) in the atomizer region, spray-dryer outlet, or stuck on the walls versus number of particle tracked. Gas flowrate = 30 $m^3.h^{-1}$ and RR-PSD = (30, 1.5).

A good convergence was obtained for 1000 droplets, i.e., a value that was systematically used for all the following simulations. Figure 12 also indicates that nearly 78% by mass of the droplets were stuck to the walls, an amount that is definitely detrimental to the drying process. This was also observed in the experiments; See Figure 14, which shows an image of the B-290 spray drying chamber after a boehmite suspension doped with a small amount of red dye was sprayed. The deposit (pink color) on the internal wall of the chamber could be easily observed.

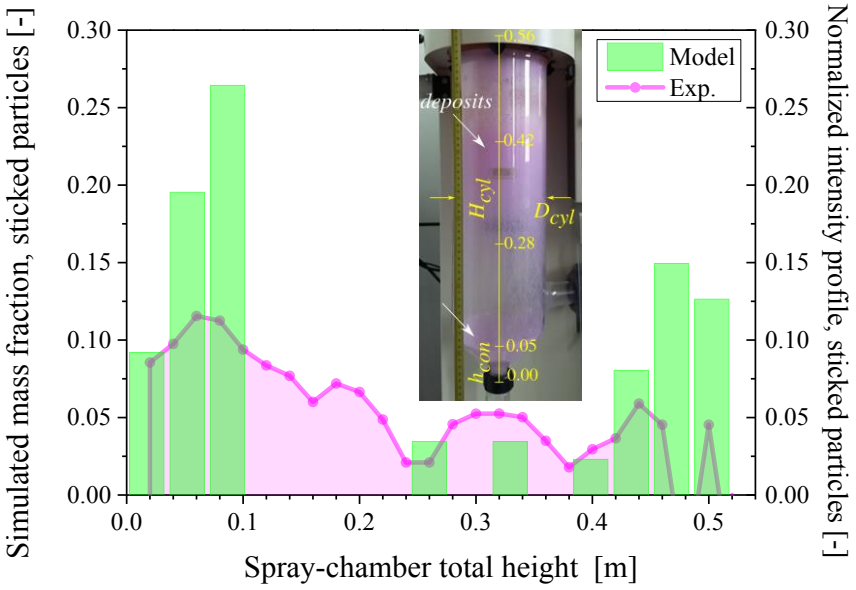

Figure 14: Comparison of numerical predictions for the axial distribution of the mass fraction of droplets stuck onto the spray-chamber walls, with the corresponding intensity profile of the image of the deposit (a dye was added to the liquid suspension). The parameters used were the same as those presented in Figure 13.

By extracting and normalizing the intensity profile of the reconstructed pink channel of this image, it is possible to evaluate, to some extent, the density of this deposit. In Figure 14, the corresponding intensity profile is compared with the numerically simulated axial distribution of the mass fraction of the droplets wetting the wall of the spray drying chamber. The correlation is rather qualitative; however, the trends are the same. The quantity of the deposit was maximum at the top of the chamber (i.e., in the atomization region, where droplet–wall collisions were expected to be maximum owing to the ballistic effects), and at the bottom part of the spray- drying chamber (conical and outlet regions), where gas recirculation is significant (see Figure 12 f).

The proposed model allows, for instance, comparing the influence of (a) the initial diameter of the sprayed droplets and (b) the gas flow rate on the distribution of the particle mass fraction, see Figure 15. It was found that the mass fraction of the droplets wetting the wall increased with the initial droplet size. After the results shown in Figure 14, this observation definitively demonstrates that the spray cone angle

is too important. The B-290 gives only access to the mass fraction of the particle yield at the outlet of the dryer. By collecting different particle samples, this value was estimated to be 0.25 ± 0.05, which was in good agreement with a numerical simulation value of 0.22 ± 0.005, as estimated for the same conditions (gas flowrate of 30 $m^3.h^{-1}$ and RR-PSD (30, 1.5)). The same agreement was found for the size of the particle exiting the chamber, as shown in Figure 11. This figure depicted the corresponding PSDs in curve (4), which represented the raw numerical results with RR-PSD fitting parameters of (13, 2.3) µm, and in curve (5), which represented the raw experimental data with RR-PSD fitting parameters of (8, 2.5) µm.

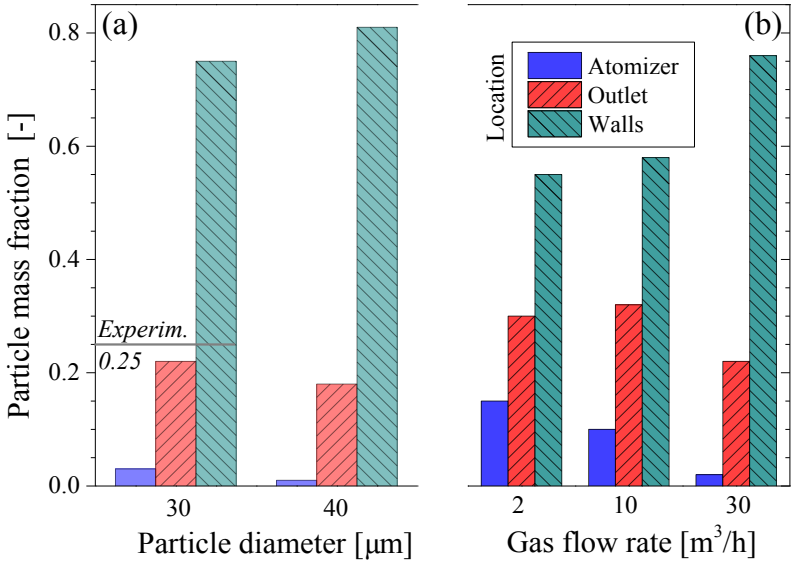

Figure 15: Distribution of the particle mass fractions (yields) in the atomizer region, spray-dryer outlet, or on the inner wall of the spray-dryer chamber: (a) influence of the initial droplet size for two cases with RR-PSDs of (40, 1.5) and (30, 1.5) µm, and a gas flow rate of 30 m^3/h; (b) influence of the gas flowrate, for an initial RR-PSD of (30, 1.5).

5 Conclusion

The predictions of the single-particle drying model, in term of the droplet shrinking process, was found to be in good agreement with

experimental data collected on a single-droplet in acoustic levitation. Its predictions on droplet buckling and particle drying processes, based on some information known a priori (mostly, the concentration limit for crust formation and deformation coefficient), were found to be less satisfactory, albeit acceptable. To pursue further on this aspect, it is essential to model the pressure drop and mechanical constraints within the crust. It is also necessary to develop new experimental diagnoses that allow the probing of the internal structure of the droplets, especially the crust formation, in real-time, e.g., (Jakubczyk et al., 2013; Lamadie et al., 2012; Onofri et al., 1999; Onofri et al., 1995). The latter improvement is already underway. The full spray drying model allows accounting for the droplet drying process, in addition to the geometry, gas flows, and atomization conditions in a realistic spray dryer. Its predictions, in terms of particle mass fraction distribution in the dryer and the PSD, agree with the experimental data collected on the mini spray dryer B-290. However, although the B-290 is widely used in the literature, its limited operating flexibility, excessive wall fouling, and a lack of accessible data make it difficult to perform a complete validation of any spray drying model. The correction of the aforementioned experimental limitations is a part of the perspectives gained from this work. Nevertheless, the results and validations reported here already confirm the potential of the modeling approach introduced in the present work, especially in terms of optimizing the spray dryer's performance.

Nomenclature

A	surface area of the droplet	m^2
A^{wet}	surface area of the wetted core in the droplet	m^2
a_w	water activity coefficient	m^2
C_{sol}	solid concentration in a layer	mol/m^3
C_D	drag coefficient	-
C_{wat}^{gas}	water concentration in the surrounding gas phase	mol/m^3
C_{sol}^{lim}	limit solid concentration of crust formation	mol/m^3

C_{wat}	liquid water concentration in a layer	mol/m^3
$C_{wat}^{vap,surf}$	water vapour concentration at the shrinking core surface	mol/m^3
$C_{wat}^{vap,sat}$	water vapour concentration at the droplet surface	mol/m^3
D	particle diameter (spray dryer oulet)	m
d_p	droplet diameter	m
d_r	layer thickness	m
D_{wat}^{vap}	diffusion coefficient of water vapor	m^2/s
D_{sol}	solid diffusion coefficient	m^2/s
E_b	activation energy	J/mol
k_{gs}	external gas-solid mass transfer coefficient	m/s
k_{gs}^{app}	apparent transfer coefficient representative to diffusion in the porous dry zone	m/s
k_{gs}^{global}	global external mass transfer coefficient	m/s
L_{wat}	latent heat of water vaporization	kg/mol
M_{wat}	water molecular weight	kg/mol
m	mass droplet	kg
M_{sol}	solid molecular weight	kg/mol
n_{wat}	moles of water in a layer	Mol
n_{wat}^{R}	moles of water in the outer layer	Mol
n_{sol}	moles of solid in a layer	mol
$P_{wat}^{vap,sat}$	water vapor pressure above the suspension	Pa
P_{wat}^{free}	free water vapor pressure	Pa
Q_{wat}^{vap}	volumetric flowrate of liquid water vaporized	m
R_{core}	liquid core radius	m
R_{tor}	torus geometrical parameter	m
r_{tor}	torus geometrical parameter	m
R	droplet radius at a given time t	m
R_{cru}	spherical droplet radius when crust starts to be formed	m
R_{gas}	gas constant	J/K/mol
Re	Reynolds number	
r	radial position in the droplet	m
Sc	Schmidt number	-
r_{sol}	colloid radius	m
T_d	droplet temperature (wet bulb temperature)	K
T	gas temperature	K
t	time	s
V_{lay}	layer volume	m^3
ϑ	velocity	m/s
V_{sol}	volume of solid in a droplet layer	m^3
V_{wat}	volume of liquid water in a droplet layer	m^3

V_{gas}	gas volume in a layer	m^3
V_{tor}	droplet volume when buckling to a torus	m^3

Greek symbols

α_{def}	deformation coefficient	-
α_{gs}	correcting factor of the external mass transfer coefficient for experiments done with the levitator	-
δ	crust thickness	m
β	slope of D^2 law	m^2/s
ε	crust porosity	-
ε_{gas}	gas holdup in a layer	-
ΔT	temperature difference along the droplet radius	K
μ_g	gas viscosity	Pa.s
λ	thermal conductivity	W/m/K
ρ_{sol}	solid density	kg/m^3
ρ_{sus}^{lim}	limit suspension density for crust formation	kg/m^3
ρ_{sus}	suspension density	kg/m^3
ρ_{wat}	liquid water density	kg/m^3
ρ_{gel}	gel density	kg/m^3
τ	tortuosity	-
θ_l	limit angle	rad

Acknowledgements

This work was partially funded by the French National Research Agency (ANR) under grant numbers ANR-13-BS09-0008-02, Labex MEC (ANR-11-LABX-0092), and A*MIDEX (ANR-11-IDEX-0001-0).

References

Ali Al Zaitone, B., Tropea, C., 2011. Evaporation of pure liquid droplets: Comparison of droplet evaporation in an acoustic field versus glass-filament. Chem. Eng. Sci. 66, 3914-3921.

Ali, M., Mahmud, T., Heggs, P.J., Ghadiri, M., Bayly, A., Ahmadian, H., Juan, L.M.d., 2015. CFD Simulation of a Counter-current Spray Drying Tower with Stochastic Treatment of Particle-wall Collision. Procedia Engineering 102, 1284-1294.

Blandamer, M.J., Engberts, J.B.F.N., Gleeson, P.T., Reis, J.C.R., 2005. Activity of water in aqueous systems; A frequently neglected property. Chemical Society Reviews 34, 440-458.

Bonazzi, C., Dumoulin, E., 2014. Quality Changes in Food Materials as Influenced by Drying Processes, in: Tsotsas, E., Mujumdar, A.S. (Eds.), Modern Drying Technology. John Wiley & Sons, Ltd, pp. 1-20.

Brenn, G., Deviprasath, L.J., Durst, F., Fink, C., 2007. Evaporation of acoustically levitated multi-component liquid droplets. International Journal of Heat and Mass Transfer 50, 5073-5086.

Cheong, H. W., Jeffreys, G. V., Mumford, C. J., 1986. A receding interface model for the drying of slurry droplets, AIChE Journal 32, Issue8, 1334-1346.

Cheow, W.S., Li, S., Hadinoto, K., 2010. Spray drying formulation of hollow spherical aggregates of silica nanoparticles by experimental design. Chemical Engineering Research and Design 88, 673-685.

Cotabarren, I.M., Bertín, D., Razuc, M., Ramírez-Rigo, M.V., Piña, J., 2018. Modelling of the spray drying process for particle design. Chemical Engineering Research and Design 132, 1091-1104.

Couderc, J.-P., 2017. Phénomènes de transfert en génie des procédés.

Crank, J., 1975. The mathematics of diffusion. Clarendon Press, Oxford.

Daubersies, L.S.V., 2012. Séchage de fluides complexes en géométrie confinée. Université Bordeaux 1, Bordeaux, France.

Fdida, N., Blaisot, J.-B., 2010. Drop size distribution measured by imaging: determination of the measurement volume by the calibration of the point spread function. Meas. Sci. Technol. 21, 025501.

Fu, N., Wai Woo, M., Qi Lin, S.X., Zhou, Z., Dong Chen, X., 2011. Reaction Engineering Approach (REA) to model the drying kinetics of droplets with different initial sizes—experiments and analyses. Chem. Eng. Sci. 66, 1738-1747.

Fu, N., Woo, M.W., Selomulya, C., Chen, X.D., 2013. Shrinkage behaviour of skim milk droplets during air drying. Journal of Food Engineering 116, 37-44.

Gaubert, Q., 2017. Caractérisation et modélisation des phénomènes gouvernant le séchage par atomisation de suspensions colloïdales Aix-Marseille University, Marseille, France., Marseille.

Handscomb, C.S., Kraft, M., Bayly A.E., 2009. A new model for the drying of droplets containing suspended solids, Chemical Engineering Science 64, 628- 637.

Hu, H., Larson, R.G., 2002. Evaporation of a Sessile Droplet on a Substrate. The Journal of Physical Chemistry B 106, 1334-1344.

Jakubczyk, D., Derkachov, G., Kolwas, M., Kolwas, K., 2013. Combining weighting and scatterometry: Application to a levitated droplet of suspension. J. Quant. Spectrosc. Radiat. Transf. 126, 99-104.

Johnson, P.J., Zyvoloski, G.A., Stauffer, P.H., 2019. Impact of a Porosity-Dependent Retention Function on Simulations of Porous Flow. Transport in Porous Media 127, 211-232.

Jubaer, H., Afshar, S., Xiao, J., Dong, X., Selomulya, C., Wai, M., 2018. On the importance of droplet shrinkage in CFD-modeling of spray drying. Drying Technology 36, 1785-1801.

Lamadie, F., Bruel, L., Himbert, M., 2012. Digital holographic measurement of liquid–liquid two-phase flows. Opt. Lasers Eng. 50, 1716-1725.

Langrish, T.A.G., 2007. New Engineered Particles from Spray Dryers: Research Needs in Spray Drying. Drying Technology 25, 971-983.

Langrish, T.A.G., Fletcher, D.F., 2003. Prospects for the Modelling and Design of Spray Dryers in the 21st Century. Drying Technology 21, 197-215.

Lauga, E., Brenner, M.P., 2004. Evaporation-Driven Assembly of Colloidal Particles. Phys. Rev. Lett. 93, 238301.

Laurence, D.R., Uribe, J.C., Utyuzhnikov, S.V., 2005. A robust formulation of the v2−f model. Flow, Turbulence and Combustion 73, 169-185.

Lebas, R., Menard, T., Beau, P.-A., Berlemont, A., Demoulin, F.-X., 2009. Numerical simulation of primary break-up and atomization: DNS and modelling study. International Journal of Multiphase Flow 35, 247-260.

Lefebvre, A., McDonell, V., 2017. Atomization and Sprays. CRC Press, Boca Raton.

Lintingre, É., Ducouret, G., Lequeux, F., Olanier, L., Périé, T., Talini, L., 2015. Controlling the buckling instability of drying droplets of suspensions through colloidal interactions. Soft Matter 11, 3660-3665.

Lintingre, E., Lequeux, F., Talini, L., Tsapis, N., 2016. Control of particle morphology in the spray drying of colloidal suspensions. Soft Matter 12, 7435-7444.

Maconi, G., Penttilä, A., Kassamakov, I., Gritsevich, M., Helander, P., Puranen, T., Salmi, A., Hæggström, E., Muinonen, K., 2018. Non-destructive controlled single-particle light scattering measurement. J. Quant. Spectrosc. Radiat. Transf. 204, 159-164.

Melling A., 1997. Tracer particles and seeding for particle image velocimetry. Meas. Sci. Technol. 8, 1406-1416.

Mezhericher, M., Levy, A., Borde, I., 2010. Theoretical Models of Single Droplet Drying Kinetics: A Review. Drying Technology, 28:2, 278-293

Miglani, A., Basu, S., 2015. Sphere to ring morphological transformation in drying nanofluid droplets in a contact-free environment. Soft Matter 11, 2268-2278.

Mujumdar, Arun S. ed. John Wiley & Sons, Ltd, pp. 231-294.Oakley, D.E., 2004. Spray Dryer Modeling in Theory and Practice. Drying Technology 22, 1371-1402.

Onofri, F., Barbosa, S., 2012. Chapter II: Optical particle characterization, in: Boutier, A. (Ed.), Laser Metrology in Fluid Mechanics. Wiley-ISTE, London.

Onofri, F., Bergougnoux, L., Firpo, J.-L., Misguich-Ripault, J., 1999. Size, velocity, and concentration in suspension measurements of spherical droplets and cylindrical jets. Appl. Opt. 38, 4681-4690.

Onofri, F., Gréhan, G., Gouesbet, G., 1995. Electromagnetic scattering from a multilayered sphere located in an arbitrary beam. Appl. Opt. 34, 7113-7124.

Onofri, F.R.A., Barbosa, S., Touré, O., Woźniak, M., Grisolia, C., 2013. Sizing highly-ordered buckyball-shaped aggregates of colloidal nanoparticles by light extinction spectroscopy. J. Quant. Spectrosc. Radiat. Transf. 126, 160-168.

Onofri, F.R.A., Ren, K.F., Sentis, M., Gaubert, Q., Pelcé, C., 2015. Experimental validation of the vectorial complex ray model on the inter-caustics scattering of oblate droplets. Opt. Express 23, 15768-15773.

Pauchard, L., Couder, Y., 2004. Invagination during the collapse of an inhomogeneous spheroidal shell. Europhys. Lett. 66, 667-673.

Pinto, M., Kemp, I., Bermingham, S., Hartwig, T., Bisten, A., 2014. Development of an axisymmetric population balance model for spray drying and validation against experimental data and CFD simulations. Chemical Engineering Research and Design 92, 619-634.

Poozesh, S., Lu, K., Marsac, P.J., 2018. On the particle formation in spray drying process for bio-pharmaceutical applications: Interrogating a new model via computational fluid dynamics. International Journal of Heat and Mass Transfer 122, 863-876.

Ranz, W., Marshall, W., 1952. Evaporation from Drops. Chemical Engineering Progress 48, 141-146.

Reuge, N., Caussat, B., 2007. A dimensionless study of the evaporation and drying stages in spray pyrolysis. Computers & Chemical Engineering 31, 1088-1099.

Saha, A., Basu, S., Suryanarayana, C., Kumar, R., 2010. Experimental analysis of thermo-physical processes in acoustically levitated heated droplets. International Journal of Heat and Mass Transfer 53, 5663-5674.

Sen, D., Bahadur, J., Mazumder, S., Bhattacharya, S., 2012. Formation of hollow spherical and doughnut microcapsules by evaporation induced self-assembly of nanoparticles: effects of particle size and polydispersity. Soft Matter 8, 10036-10044.

Sen, D., Melo, J.S., Bahadur, J., Mazumder, S., Bhattacharya, S., Ghosh, G., Dutta, D., D'Souza, S.F., 2010. Buckling-driven morphological transformation of droplets of a mixed colloidal suspension during evaporation-induced self-assembly by spray drying. The European Physical Journal E 31, 393-402.

Singh, A., Van den Mooter, G., 2016. Spray drying formulation of amorphous solid dispersions. Advanced Drug Delivery Reviews 100, 27-50.

Sirignano, W. A. , Author, Edwards, Chris F. , Reviewer, 2000. Fluid Dynamics and Transport of Droplets and Sprays. Journal of Fluids Engineering 122, 189-190.

Sobac, Benjamin; Dehaeck, Sam; Bouchaudy, Anne; Salmon, Jean-Baptiste (2020) Collective diffusion coefficient of a charged colloidal dispersion: interferometric measurements in a drying drop. In : Soft matter, vol. 16, n° 35, p. 8213–8225.

Sosnik, A., Seremeta, K.P., 2015. Advantages and challenges of the spray-drying technology for the production of pure drug particles and drug-loaded polymeric carriers. Advances in Colloid and Interface Science 223, 40-54.

Sperling, M., Gradzielski, M., 2017. Droplets, Evaporation and a Superhydrophobic Surface: Simple Tools for Guiding Colloidal Particles into Complex Materials. Gels 3.

Style, R.W., Peppin, S.S.L., 2010. Crust formation in drying colloidal suspensions. Proceedings of the Royal Society A: Mathematical, Physical and Engineering Science.

Timoshenko, S.P.,1936.Theory of Elastic Stability. First ed. McGraw-Hill, New-York.Tirumkudulu, M.S., 2018. Buckling of a drying colloidal drop. Soft Matter 14, 7455-7461.

Walton, D.E., 2000. The morphology of spray-dried particles a qualitative view. Drying Technology 18, 1943-1986.

Walton, D.E., Mumford, C.J., 1999. The Morphology of Spray-Dried Particles: The Effect of Process Variables upon the Morphology of Spray-Dried Particles. Chemical Engineering Research and Design 77, 442-460.

Walzel, P., Furuta, T., 2011. Morphology and Properties of Spray-Dried Particles, Modern Drying Technology, Tsotsas, Evangelos

Wei, Y., Deng, W., Chen, Ruey-Hung, Effects of internal circulation and particle mobility during nanofluiddroplet evaporation, 2016. International Journal of Heat and Mass Transfer, 103, 1335-1347.

Yarin, A.L., Brenn, G., Kastner, O., Rensink , D., Tropea, C., 1999. Evaporation of acoustically levitated droplets. J. Fluid Mech. 399, 151-204.

Yarin, A.L., Brenn, G., Kastner, O., Tropea, C., 2002. Drying of acoustically levitated droplets of liquid-solid suspensions: Evaporation and crust formation. Physics of Fluids 14, 2289.

Yarin, A.L., Pfaffenlehner, M., Tropea, C., 1998. On the acoustic levitation of droplets. Journal of Fluid Mechanics 356, 65-91.

Yu, H., Xu, F., Tropea, C., 2013. Optical caustics associated with the primary rainbow of oblate droplets: simulation and application in non-sphericity measurement. Opt. Express 21, 25761-25771.